LETTER

doi:10.1038/nature14399

The formation and fate of internal waves in the South China Sea

Matthew H. Alford[1,2], Thomas Peacock[3], Jennifer A. MacKinnon[1], Jonathan D. Nash[4], Maarten C. Buijsman[5], Luca R. Centuroni[1], Shenn-Yu Chao[6], Ming-Huei Chang[7], David M. Farmer[8]†, Oliver B. Fringer[9], Ke-Hsien Fu[10], Patrick C. Gallacher[11], Hans C. Graber[12], Karl R. Helfrich[13], Steven M. Jachec[14], Christopher R. Jackson[15], Jody M. Klymak[16], Dong S. Ko[11], Sen Jan[7], T. M. Shaun Johnston[1], Sonya Legg[17], I-Huan Lee[10], Ren-Chieh Lien[2], Matthieu J. Mercier[18], James N. Moum[4], Ruth Musgrave[1], Jae-Hun Park[19], Andrew I. Pickering[2,3], Robert Pinkel[1], Luc Rainville[2], Steven R. Ramp[20], Daniel L. Rudnick[1], Sutanu Sarkar[21], Alberto Scotti[22], Harper L. Simmons[23], Louis C. St Laurent[13], Subhas K. Venayagamoorthy[24], Yu-Huai Wang[10], Joe Wang[7], Yiing J. Yang[7], Theresa Paluszkiewicz[25] & Tswen-Yung (David) Tang[7]

Internal gravity waves, the subsurface analogue of the familiar surface gravity waves that break on beaches, are ubiquitous in the ocean. Because of their strong vertical and horizontal currents, and the turbulent mixing caused by their breaking, they affect a panoply of ocean processes, such as the supply of nutrients for photosynthesis[1], sediment and pollutant transport[2] and acoustic transmission[3]; they also pose hazards for man-made structures in the ocean[4]. Generated primarily by the wind and the tides, internal waves can travel thousands of kilometres from their sources before breaking[5], making it challenging to observe them and to include them in numerical climate models, which are sensitive to their effects[6,7]. For over a decade, studies[8–11] have targeted the South China Sea, where the oceans' most powerful known internal waves are generated in the Luzon Strait and steepen dramatically as they propagate west. Confusion has persisted regarding their mechanism of generation, variability and energy budget, however, owing to the lack of *in situ* data from the Luzon Strait, where extreme flow conditions make measurements difficult. Here we use new observations and numerical models to (1) show that the waves begin as sinusoidal disturbances rather than arising from sharp hydraulic phenomena, (2) reveal the existence of >200-metre-high breaking internal waves in the region of generation that give rise to turbulence levels >10,000 times that in the open ocean, (3) determine that the Kuroshio western boundary current noticeably refracts the internal wave field emanating from the Luzon Strait, and (4) demonstrate a factor-of-two agreement between modelled and observed energy fluxes, which allows us to produce an observationally supported energy budget of the region. Together, these findings give a cradle-to-grave picture of internal waves on a basin scale, which will support further improvements of their representation in numerical climate predictions.

Internal gravity waves are propagating disturbances of the ocean's density stratification. Their physics resembles that of surface gravity waves but with buoyancy rather than gravity providing their restoring force—making them much larger (amplitudes of tens to hundreds of metres instead of less than ten metres) and slower (hours instead of seconds). Generated primarily by tidal flow past seafloor topography and winds blowing on the sea surface, and typically having multi-kilometre-scale horizontal wavelengths, their estimated terawatt of deep-sea dissipation is understood to play a crucial role in the ocean's global redistribution of heat and momentum[12]. A major challenge is to improve our understanding of internal wave generation, propagation, steepening and dissipation, so that the role of internal waves can be more accurately incorporated into climate models.

The internal waves that originate from the Luzon Strait on the eastern margin of the South China Sea are the largest waves documented in the global oceans (Fig. 1). As the waves propagate west from the Luzon Strait they steepen dramatically (Fig. 1a), producing distinctive solitary wave fronts evident in sun glint and synthetic aperture radar images from satellites (Fig. 1b). When they shoal onto the continental slope to the west, the downward displacement of the ocean's layers associated with these solitary waves can exceed 150 m in 5 min (ref. 8). The scale of these waves means that they pose hazards for underwater navigation and offshore drilling[4], and supply nutrients from the deep ocean that nourish coral reefs[1] and pilot whale populations that forage in their wakes[13].

Over the past decade a number of field studies have been conducted in the region; this work has been comprehensively reviewed[10,11]. All of these studies, however, focused on the propagation of the internal waves across the South China Sea and their interactions with the continental shelf of China. Until the present study there have been no substantial *in situ* data gathered at the generation site of the Luzon Strait, in large part because of the extremely challenging operating conditions. A consequence has been persistent confusion regarding the nature of the mechanism of wave generation[11] with an underlying cause being the sensitivity of the models employed to the system parameters, such as the chosen transect for a two-dimensional model, the linear internal wave speed or the assumed location of the waves' origin within the Luzon Strait. Furthermore, the lack of *in situ* data from the Luzon Strait has meant an inability to test numerical predictions of energy budgets[9] and no knowledge of the impact of the Kuroshio Current on the emergence of internal solitary waves[11].

The goal of the Internal Waves in Straits Experiment (IWISE) is to obtain the first comprehensive *in situ* data set from the Luzon Strait, which in combination with high-resolution three-dimensional numerical modelling supports a cradle-to-grave picture of the life cycle of the

[1]Scripps Institution of Oceanography, University of California San Diego, La Jolla, California 92037, USA. [2]University of Washington, Seattle, Washington 98105, USA. [3]Massachusetts Institute of Technology (MIT), Cambridge, Massachusetts 02139, USA. [4]Oregon State University, Corvallis, Oregon 97370, USA. [5]University of Southern Mississippi, Stennis Space Center, Mississippi 39529, USA. [6]University of Maryland, Cambridge, Maryland 21613, USA. [7]Institute of Oceanography, National Taiwan University, Taipei 10617, Taiwan. [8]University of Rhode Island, Rhode Island 02882, USA. [9]Stanford University, Stanford, California 94305, USA. [10]National Sun-Yat Sen University, Kaohsiung 80424, Taiwan. [11]Naval Research Laboratories (NRL), Stennis Space Center, Mississippi 39529, USA. [12]University of Miami, Miami, Florida 33149, USA. [13]Woods Hole Oceanographic Institution, Falmouth, Massachusetts 02543, USA. [14]Florida Institute of Technology, Melbourne, Florida 32901, USA. [15]Global Ocean Associates, Alexandria, Virginia 22310, USA. [16]University of Victoria, Victoria, British Columbia V8W 3P6, Canada. [17]Princeton University, New Jersey 08542, USA. [18]Institut de Mécanique des Fluides de Toulouse, Toulouse 31400, France. [19]Korea Institute of Ocean Science and Technology, Ansan 426–744, South Korea. [20]Soliton Ocean Services, Carmel, California 93924, USA. [21]University of California San Diego, La Jolla, California 92037, USA. [22]University of North Carolina, Chapel Hill, North Carolina 25599, USA. [23]University of Alaska at Fairbanks, Fairbanks, Alaska 99775, USA. [24]Colorado State University, Fort Collins, Colorado 80523, USA. [25]Office of Naval Research, Arlington, Virginia, USA. †Present address: School of Earth and Ocean Sciences, University of Victoria, British Columbia V8P 5C, Canada.

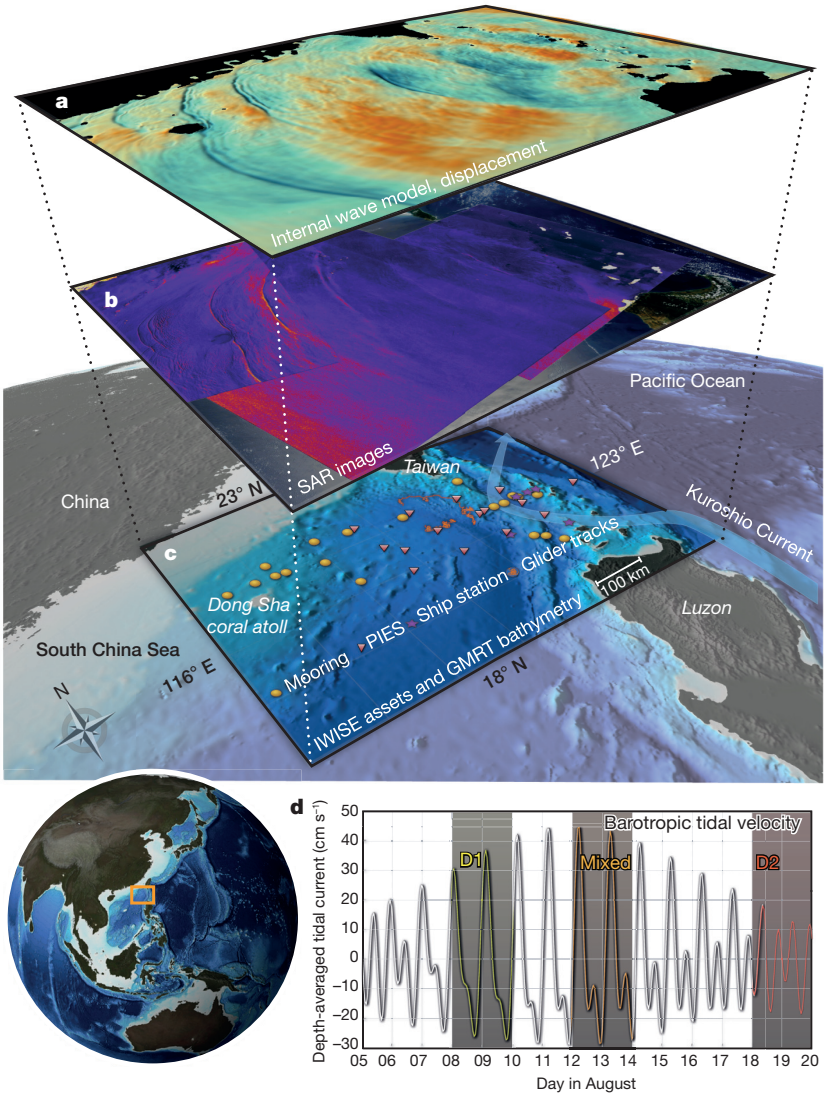

Figure 1 | Overview of internal waves in the South China Sea. **a**, Vertical displacement of ocean layers near 200 m depth from the far-field numerical simulation. Orange and blue indicate upward and downward displacements, respectively. **b**, A collage of synthetic aperture radar images taken on 12 August 2009, 04 August 2009 and 25 April 2005. Wave fronts are visible because they focus surface waves, increasing sea surface roughness. Red and blue correspond to greater and less surface roughness, respectively. **c**, Instrumentation deployed during IWISE. The Kuroshio Current is sketched schematically. PIES, pressure inverted echo sounder. **d**, Time series (5–20 August 2011) of depth-averaged tidal current in Luzon Strait over a spring/neap cycle, showing the presence of once-daily (diurnal, D1) and twice-daily (semidiurnal, D2) frequencies. Inset, globe showing location of Luzon Strait and South China Sea.

world's largest known oceanic internal waves. IWISE is the most substantial internal wave field programme since the Hawaiian Ocean Mixing Experiment (HOME)[14] revealed how most of the tidal losses from a complex ocean ridge system can be radiated away as nearly sinusoidal waves, with a small fraction dissipated locally. IWISE is broader in scope, however, because the radiated internal tide is nonlinear and therefore subject to additional steepening and wave-breaking processes. A pilot study was performed in the summer of 2010 to determine the feasibility of operating at desired locations[15], and the full field programme was executed throughout the summer of 2011. This Letter is a synthesis of the results from both programmes.

The internal tides derive their energy from the barotropic (surface) tide: the flow arising from astronomical forcing of the oceans by the Sun and the Moon. The barotropic tides in this region are a combination of twice-daily (semidiurnal, D2) and once-daily (diurnal, D1) motions, giving rise to a strong diurnal inequality and a fortnightly amplitude envelope caused by the interaction of lunar and solar tides (Fig. 1d). Our moorings, shipboard stations, and autonomous gliders within and to the west of the Luzon Strait reveal time-averaged westward energy fluxes of 40 ± 8 kW m^{-1} (Fig. 2a; see Methods). Such values are about 100 times typical open-ocean values[16] and exceed any other known generation site around the world[15]. The measured fluxes agree to within a factor of two in magnitude and ±30° in direction with the predictions of our far-field numerical model (see Methods), as well as previous numerical predictions[9].

The total energy flux in the northern section of the Luzon Strait shows a clockwise pattern between the tall east and west ridges (Fig. 2a). This feature exists because the double-ridge structure creates a 100-km-scale resonant cavity for the ~100-km wavelength semi-diurnal internal tide[17]; the existence of this resonant cavity is confirmed by observations of very high energy density but little energy flux between the two ridges, characteristic of a standing-wave pattern[15]. Tidal flow transiting the ridge in the vicinity of the Batanes Islands (Fig. 2f) gives rise to dramatic localized lee wave phenomena[18]. Shipboard time series of velocity and density, obtained at the location of the dashed lines in Fig. 2b and c, are presented in Fig. 2d. Observed vertical displacements of the ocean layers reach up to 500 m, with static instabilities >200 m high. The associated depth-integrated turbulent dissipation levels (Fig. 2e; see Methods) approach 20 W m^{-2}, exceeding open-ocean values by a factor of 1,000–10,000 (refs 12 and 15). The associated vertical mixing of quantities such as temperature and salinity is sufficiently high (>10^{-1} m^2 s^{-1})—also orders of magnitude greater than open-ocean values—that it probably plays a key part in setting large-scale circulation patterns throughout the South China Sea[19].

There was no evidence of coherent nonlinear internal waves east of 120.5° E, disproving previous conjectures that the large-amplitude internal solitary waves arise in the immediate vicinity of the Luzon Strait via a hydraulic lee wave mechanism[11]. Rather, what emerges immediately to the west of the Luzon Strait is a broad, energetic, spatially coherent, nearly sinusoidal internal tide (Figs 1a, 2a and 3a, b) at a

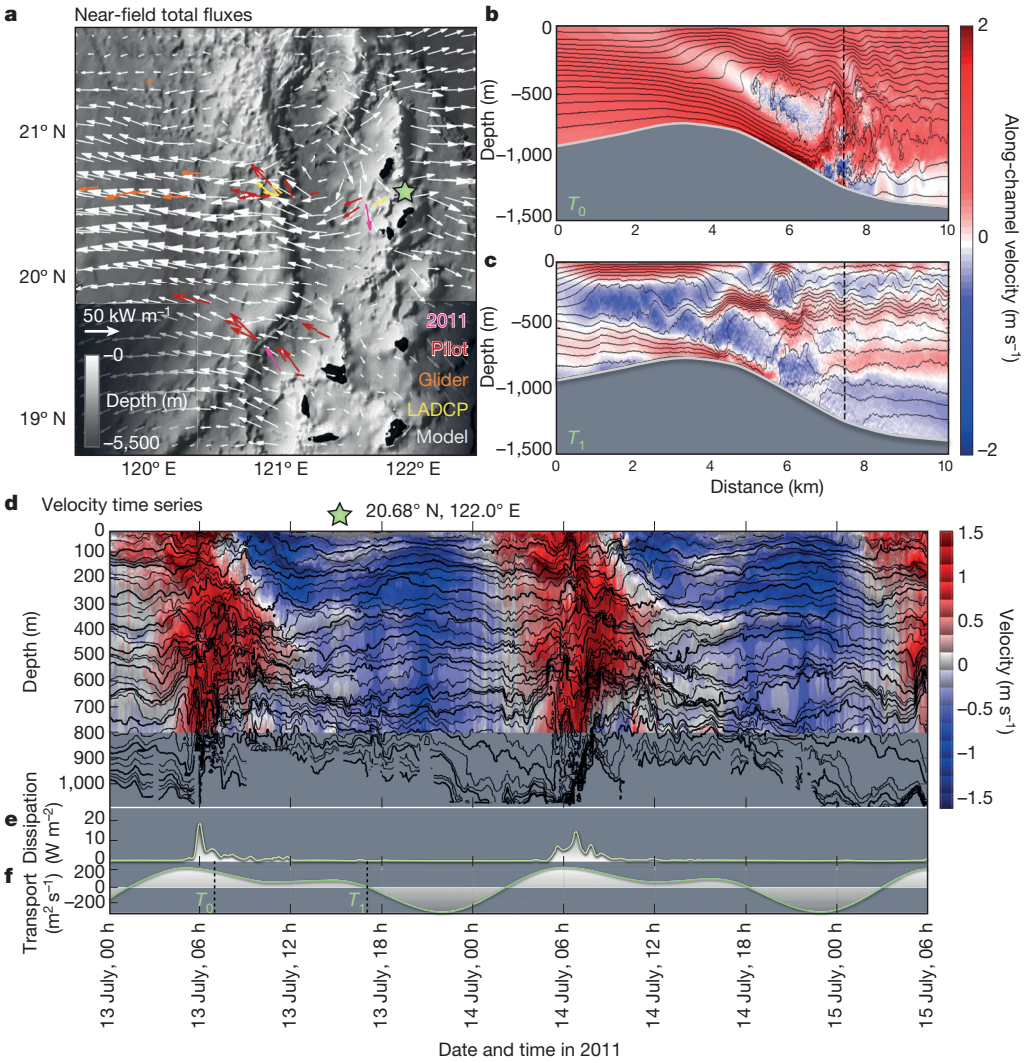

Figure 2 | Near-field processes in the Luzon Strait. **a**, Time-mean total energy flux from the near-field numerical model (white arrows) and field measurements (coloured arrows). LADCP, lowered acoustic Doppler current profiler measurements (see Methods). **b**, **c**, Snapshots from the two-dimensional model showing internal wave breaking at the location indicated in **a** by the green star, corresponding to times T_0 and T_1 indicated in **f**. Colours and lines in **b** and **c** indicate east–west velocity and density contours, respectively. **d**, Corresponding field measurements at the location of the vertical dashed line in **b** and **c**. **e**, Depth-averaged dissipation rate computed from Thorpe scales. **f**, Depth-integrated eastward tidal transport, showing the times T_0, T_1 of the frames in **b** and **c**.

combination of semidiurnal and diurnal frequencies (Fig. 1d). The structure of the wave field is dominated by 'mode 1' behaviour[15], this being the fundamental vertical mode of oscillation in which velocity in the upper few hundred metres of the ocean is in the opposite direction to, and oscillates out of phase with, the velocity in the deeper ocean (Fig. 3d). The three-dimensional structure of the ridge system within the Luzon Strait shapes the radiated semidiurnal and diurnal internal tides differently because the horizontal wavelength of the former is half that of the latter. The semi-diurnal internal tide energy flux is strongest within a beam that emanates from the central section of the Luzon Strait, between 20° N and 21° N (Fig. 3a), while a broader beam of diurnal energy flux emanates from across the central and southern sections of the Luzon Strait (Fig. 3b). These beams are also evident in the field data: characteristic diurnal energy fluxes of ~5 kW m^{-1} and ~20 kW m^{-1} were detected in the central and southern sections of the Luzon Strait, respectively, and the corresponding values for the semi-diurnal energy fluxes were ~20 kW m^{-1} and ~10 kW m^{-1} (ref. 15). These results and interpretations were furthermore supported by a rotating, large-scale laboratory experiment, using an accurate scale model of the Luzon Strait[20].

The combination of mode-1-dominated semidiurnal and diurnal internal tides sets the initial condition for the evolution of large-amplitude solitary waves[21]. Whether or not steepening occurs depends crucially on the balance between nonlinearity and rotational dispersion, which serve to enhance and reduce the steepness of the wavefronts, respectively[21,22]. When the semidiurnal internal tide dominates, nonlinearity can overcome rotational dispersion, leading to the formation of internal solitary waves around 120° E as seen in Fig. 1a, b; if diurnal forcing dominates, however, rotational dispersion tends to suppress wave formation. Other factors are the fortnightly spring/neap cycle (Fig. 1d), which sets the overall amplitude of barotropic tidal forcing in the Luzon Strait, and the interaction between the semidiurnal and diurnal tides, which can cause alternating strong and weak wave fronts[23].

Another key influence on the radiated waves is the Kuroshio Current, one of the oceans' foremost (in volume, extent and velocity) boundary currents, whose modelled lateral structure and velocities of over 0.5 m s^{-1} were confirmed by our measurements (Fig. 4a). When it intrudes into the Luzon Strait, the Kuroshio Current refracts the internal tide, profoundly affecting the subsequent propagation path of the internal waves. For example, we determined that the orientation of the semidiurnal beam was notably different during our winter 2010–2011 field study[24] compared to a previous field study in winter 2006, for which moorings were deployed near Dongsha Island[25]. No solitary waves were detected in winter by the latter study (Fig. 4b), so solitary waves were thought not to be present in the South China Sea during the wintertime. This is not the case, however, as solitary waves persisted throughout the winter of our 2010–2011 field study (Fig. 4c)[24]. Instead, we determined that during winter 2006 the Kuroshio Current was responsible for directing the semidiurnal internal tide beam, and thus the solitary waves, south of the mooring location[24].

Proceeding into the shallower waters of the Dongsha Plateau at speeds of roughly 3 m s^{-1}, the internal solitary waves begin to slow down[26]. Eventually, the wave-induced fluid velocities can exceed the

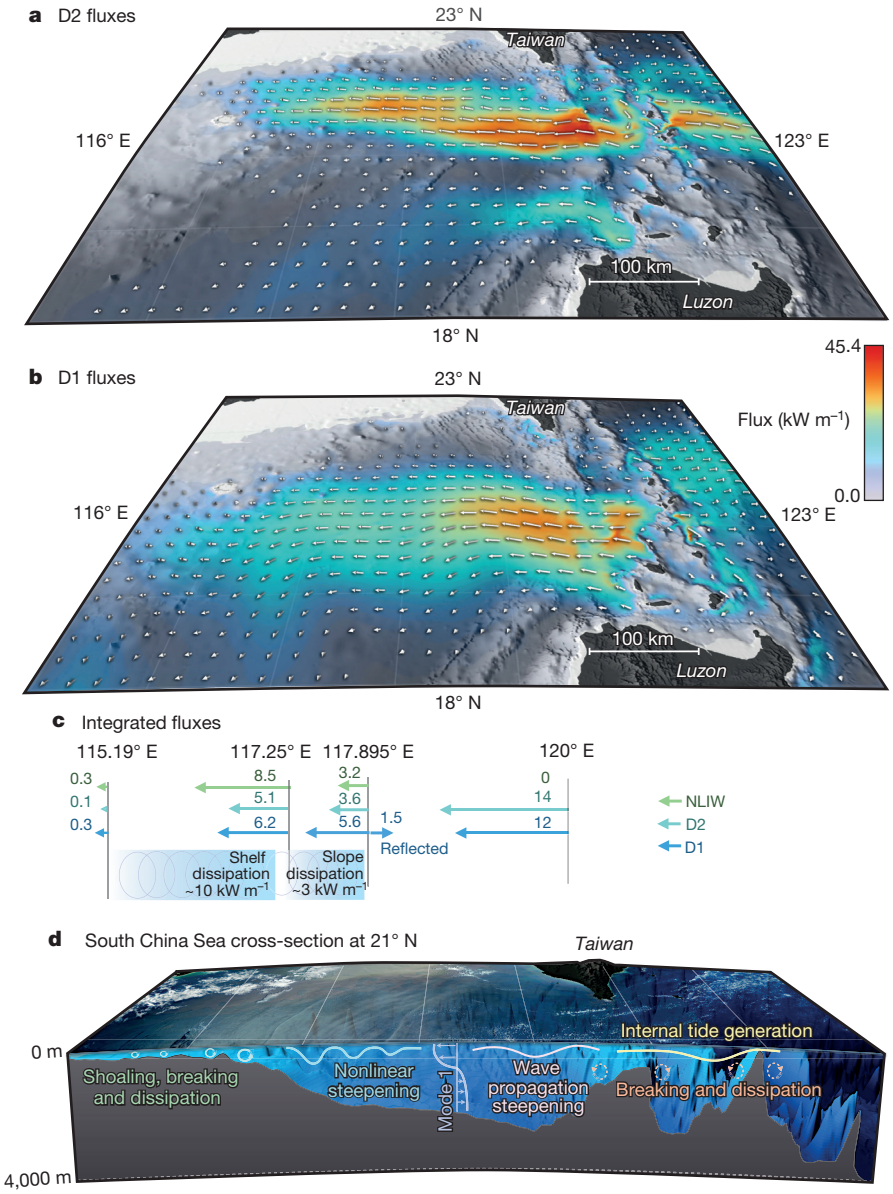

Figure 3 | Internal wave energy fluxes in the South China Sea. **a**, **b**, Semidiurnal (**a**) and diurnal (**b**) energy flux from the far-field model. **c**, Energy flux along 21° N. Arrows in **c** indicate integrated energy fluxes (numbers on arrows are fluxes in kilowatts per metre) at 21° N in the semidiurnal and diurnal internal tides and in the solitary or nonlinear internal waves (NLIW). Flux values at 120° E are from the near-field model; flux and dissipation values at 115.19° E, 117.25° E and 117.895° E are from observations (see Methods). **d**, Bathymetry along 21° N. The processes of generation, breaking, propagation, steepening and dissipation are shown schematically.

wave speed, leading to the formation of trapped cores[27], wherein fluid is carried along with the wave. At this stage, the waves vertically displace water up to 170 m, nearly 40% of the local ocean depth, in only a few minutes and have wavelengths of only a few hundred metres. The solitary waves become highly turbulent, leading to strong vertical mixing that has been postulated to contribute to the high biological productivity in the vicinity of the nearby Dongsha coral atoll[1]. We observed the waves to become convectively and shear unstable, producing vertical overturns of up to one hundred metres within the core. Measured turbulent dissipation rates are extreme, exceeding 1.5×10^{-4} W kg^{-1}, contributing to a cross-shelf integrated dissipation level of 10 kW per metre of coastline (see Methods).

The combination of IWISE numerical models and field measurements enables us to estimate an energy budget for internal waves throughout the entire South China Sea, as summarized in Fig. 3c. Our far-field model (see Methods) predicts that, out of a total conversion of 24 GW from the barotropic tide at the Luzon Strait, 15 GW are radiated to the east and west, agreeing to within a factor of two with observations; this suggests that around 40% of the energy is dissipated locally at the Luzon Strait. For comparison, our higher-resolution near-field model, which captured the generation region only, obtains a similarly high fraction of locally dissipated energy, but conversion and fluxes are about 1.8 times higher. These results suggest that the Luzon Strait is a more highly dissipative system than the Hawaiian Ridge, where only about 15% of the energy is dissipated locally[28]. Differences between the two models, however, which we attribute to model resolution and their inability to directly resolve turbulence, emphasize that further computational advances are still required for quantitative certainty.

The observed westward energy flux at 120° E is approximately equipartitioned between semidiurnal and diurnal motions, with no energy yet in the sharp wavefronts. Closer to the continental slope at 117.25° E, however, the nonlinear internal waves (NLIW) gain energy at the expense of the internal tide, and energy is more equally distributed among all three components (D1, D2 and NLIW). At the continental slope, the diurnal motions are partially reflected (eastward arrows at 117.895° E), while the steeper semidiurnal motions and nonlinear waves are transmitted, with active turbulence dissipating about 3 kW m^{-1} (ref. 29). By 115.19° E, strong dissipation due to wave breaking over the continental shelf has removed nearly all energy in the nonlinear waves and internal tides.

The comprehensive modelling and measurements of the IWISE programme have resulted in a first-order energy budget and an understanding of the key physical processes occurring in the Luzon Strait that lead to

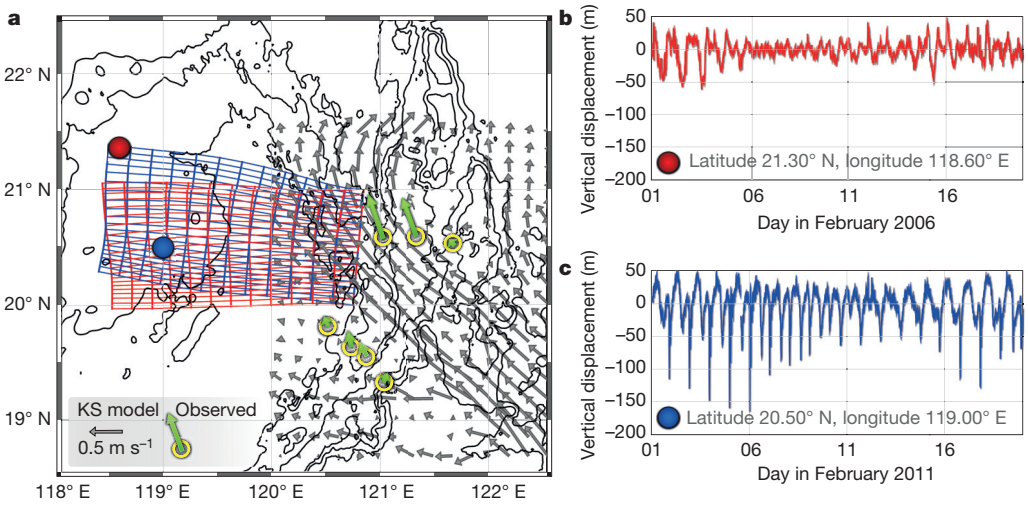

Figure 4 | The Kuroshio and its impact on wave propagation. **a**, Observed (green) and modelled (grey) Kuroshio flow during June–August 2011 in the Luzon Strait region. The meshes are modelled phase lines of internal waves during February 2006 (red) and February 2011 (blue). KS model indicates the NRL Kuroshio model (see Methods). **b**, **c**, Measured wave displacement at the locations shown in **a**. Waves were observed year-round at the southern station in 2011 (**c**), but not at the northern station in 2006 (**b**), when the Kuroshio Current deflected the internal wave paths southward (**a**, red).

the formation of the world's strongest known internal waves. Conversion from the barotropic tide leads to strong internal tides accompanied by vigorous near-field turbulence. These internal tides radiate westward through the strong Kuroshio Current, steepen into sharp wavefronts, and eventually break on the continental shelf. In spite of this clear physical picture, some questions remain, including the precise fraction of energy dissipated locally and the role of the Kuroshio Current in modulating the wave amplitudes. To improve the representation of internal waves and their associated vertical mixing in numerical climate predictions will require more sophisticated and high-resolution numerical models that can successfully capture the weakly nonlinear, non-hydrostatic, and strongly nonlinear mechanisms[30].

Online Content Methods, along with any additional Extended Data display items and Source Data, are available in the online version of the paper; references unique to these sections appear only in the online paper.

Received 9 February 2014; accepted 4 March 2015.

1. Wang, Y. H., Dai, C. F. & Chen, Y. Y. Physical and ecological processes of internal waves on an isolated reef ecosystem in the South China Sea. *Geophys. Res. Lett.* **34,** 1–5 (2007).
2. Bogucki, D., Dickey, T. & Redekopp, L. Sediment resuspension and mixing by resonantly generated internal solitary waves. *J. Phys. Oceanogr.* **27,** 1181–1196 (1997).
3. Williams, K. L., Henyey, F. S., Rouseff, D., Reynolds, S. A. & Ewart, T. Internal wave effects on high-frequency acoustic propagation to horizontal arrays—experiment and implications to imaging. *IEEE J. Oceanic Eng.* **26,** 102–112 (2001).
4. Osborne, A. R., Burch, T. L. & Scarlet, R. I. The influence of internal waves on deep-water drilling. *J. Petrol. Technol.* **30,** 1497–1504 (1978).
5. Ray, R. D. & Mitchum, G. T. Surface manifestation of internal tides generated near Hawaii. *Geophys. Res. Lett.* **23,** 2101–2104 (1996).
6. Simmons, H., Jayne, S., Laurent, L. S. & Weaver, A. Tidally driven mixing in a numerical model of the ocean general circulation. *Ocean Model.* **6,** 245–263 (2004).
7. Melet, A., Hallberg, R., Legg, S. & Polzin, K. L. Sensitivity of the ocean state to the vertical distribution of internal-tide-driven mixing. *J. Phys. Oceanogr.* **43,** 602–615 (2013).
8. Ramp, S. R. *et al.* Internal solitons in the northeastern South China Sea, part I: sources and deep-water propagation. *IEEE J. Oceanic Eng.* **29,** 1157–1181 (2004).
9. Jan, S., Lien, R. & Ting, C. Numerical study of baroclinic tides in Luzon Strait. *J. Oceanogr.* **64,** 789–802 (2008).
10. Cai, S., Xie, J. & He, J. An overview of internal solitary waves in the South China Sea. *Surv. Geophys.* **33,** 927–943 (2012).
11. Guo, C. & Chen, X. A review of internal solitary wave dynamics in the northern South China Sea. *Prog. Oceanogr.* **121,** 7–23 (2014).
12. Ferrari, R. & Wunsch, C. Ocean circulation kinetic energy: reservoirs, sources, and sinks. *Annu. Rev. Fluid Mech.* **41,** 253–282 (2009).
13. Moore, S. & Lien, R.-C. Pilot whales follow internal solitary waves in the South China Sea. *Mar. Mamm. Sci.* **23,** 193–196 (2007).
14. Rudnick, D. *et al.* From tides to mixing along the Hawaiian Ridge. *Science* **301,** 355–357 (2003).
15. Alford, M. H. *et al.* Energy flux and dissipation in Luzon Strait: two tales of two ridges. *J. Phys. Oceanogr.* **41,** 2211–2222 (2011).
16. Alford, M. H. Energy available for ocean mixing redistributed through long-range propagation of internal waves. *Nature* **423,** 159–162 (2003).
17. Buijsman, M. *et al.* Three-dimensional double-ridge internal tide resonance in Luzon Strait. *J. Phys. Oceanogr.* **44,** 850–869 (2014).
18. Pinkel, R., Buijsman, M. & Klymak, J. M. Breaking topographic lee waves in a tidal channel in Luzon Strait. *Oceanography* **25,** 160–165 (2012).
19. Qu, T., Du, Y. & Sasaki, H. South China Sea throughflow: a heat and freshwater conveyor. *Geophys. Res. Lett.* **33,** L23617 (2006).
20. Mercier, M. *et al.* Large-scale realistic modeling of M2 internal tide generation at the Luzon Strait. *Geophys. Res. Lett.* **40,** 5704–5709 (2013).
21. Helfrich, K. R. & Grimshaw, R. H. J. Nonlinear disintegration of the internal tide. *J. Phys. Oceanogr.* **38,** 686–701 (2008).
22. Farmer, D., Li, Q. & Park, J.-H. Internal wave observations in the South China Sea: the role of rotation and nonlinearity. *Atmosphere-Ocean* **47,** 267–280 (2009).
23. Li, Q. & Farmer, D. The generation and evolution of nonlinear internal waves in the deep basin of the South China Sea. *J. Phys. Oceanogr.* **41,** 1345–1363 (2011).
24. Park, J.-H. & Farmer, D. M. Effects of Kuroshio intrusions on nonlinear internal waves in the South China Sea during winter. *J. Geophys. Res.* **118,** 7081–7094 (2013).
25. Ramp, S. R., Yang, Y. & Bahr, F. L. Characterizing the nonlinear internal wave climate in the Northeastern South China Sea. *Nonlinear Process. Geophys.* **17,** 481–498 (2010).
26. Alford, M. H. *et al.* Speed and evolution of nonlinear internal waves transiting the South China Sea. *J. Phys. Oceanogr.* **40,** 1338–1355 (2010).
27. Lien, R.-C., Henyey, F., Ma, B. & Yang, Y.-J. Large-amplitude internal solitary waves observed in the northern South China Sea: properties and energetics. *J. Phys. Oceanogr.* **44,** 1095–1115 (2014).
28. Klymak, J. M. *et al.* An estimate of tidal energy lost to turbulence at the Hawaiian Ridge. *J. Phys. Oceanogr.* **36,** 1148–1164 (2006).
29. Klymak, J. M., Alford, M. H., Pinkel, R., Lien, R. C. & Yang, Y. J. The breaking and scattering of the internal tide on a continental slope. *J. Phys. Oceanogr.* **41,** 926–945 (2011).
30. Vitousek, S. & Fringer, O. B. Physical vs. numerical dispersion in nonhydrostatic ocean modeling. *Ocean Model.* **40,** 72–86 (2011).

Acknowledgements This article is dedicated to the memory of author T.-Y. Tang. Our work was supported by the US Office of Naval Research and the Taiwan National Science Council. We are indebted to the captains and crew of all of the research vessels that supported this work, as well as to the technical staff of the seagoing institutions. Without the skill and hard work of all of these people, these observations would not have been possible.

Author Contributions All authors contributed to the paper in multiple ways. Primary writing: M.H.A., T. Peacock, J.A.M. & J.D.N. Synthesis and overall coordination: T. Paluszkiewicz & T.-Y.T. Energy flux calculations: M.H.A. & A.I.P. Energy budget calculation: M.H.A., M.C.B., M.-H.C., R.-C.L., J.M.K. & L.C.S.L. Near-field moorings and calculations: M.H.A., A.I.P., L.R., J.D.N., J.N.M. & M.-H.C. Far-field moorings and calculations: L.R.C., M.-H.C., R.-C.L., S.R.R., Y.J.Y. & T.-Y.T. Near-field CTD measurements (Fig. 2d): R.P. & R.M. Near-field lowered acoustic Doppler current profiler measurements: M.H.A., J.D.N., J.A.M., L.R., H.L.S., A.I.P & R.M. Pressure inverted echo sounder measurements: D.M.F., J.-H.P., Y.J.Y. & M.H.A. Microstructure measurements: L.C.S.L., K.-H.F., H.L.S. & Y.-H.W. Remote sensing: C.R.J. & H.C.G. Theory: K.R.H. & D.M.F. Glider measurements: T.M.S.J. & D.L.R. Regional contextualization and logistical support: S.-Y.C., I-H.L., S.R.R., J.W., Y.J.Y. & T.-Y.T. Far-field modelling: S.J. & H.L.S. Two-dimensional modelling: J.M.K., S.S., S.M.J., A.S., R.M. & K.V. Near-field modelling: M.C.B., O.B.F., S.L. & S.M.J. Kuroshio modelling: P.C.G., S.J. & D.S.K. Laboratory measurements: T. Peacock & M.J.M.

Author Information Reprints and permissions information is available at www.nature.com/reprints. The authors declare no competing financial interests. Readers are welcome to comment on the online version of the paper. Correspondence and requests for materials should be addressed to M.H.A. (malford@ucsd.edu).

METHODS

Numerical models. Several numerical models were used in this paper, representing varying degrees of resolution, domain size and resolved processes. Four three-dimensional models with realistic bathymetry and stratification were employed, namely a 'far-field' model, a 'near-field' model, and two 'Kuroshio' models. A two-dimensional (horizontal–vertical) model was also used.

The three-dimensional models were used to simulate basin-scale waves, near-field physical processes, and the role of the Kuroshio Current, respectively. All were forced with predictions using eight tidal constituents (K1, O1, P1, Q1, K2, M2, N2 and S2) from a barotropic tidal model, TPXO7.2 (ref. 31), which was validated against measured currents in the region in this and a previous experiment[15,25]. Bathymetry was from multibeam depth soundings where available, and from the 30-arcsecond database[32] elsewhere. Stratification was horizontally uniform in the far-field and near-field models, obtained from the generalized digital environmental model database (GDEM) climatology for the month of August[33] for the far-field model and from August 2010 field data for the near-field model. Stratification in the Kuroshio models was from larger-scale data-assimilating regional simulations.

The far-field model (Figs 1a and 3a, b) is based on the Hallberg isopycnal model[34] and encompasses the entire South China Sea with a spatial resolution of 2 km and 40 layers in the vertical[35]. The near-field model data (Fig. 2a), with a horizontal resolution of 250 m, were generated using a 154-layer implementation of the MIT global climate model (MITgcm; ref. 36), based on the configuration in ref. 10. The MITgcm was also used to generate the two-dimensional numerical results presented in Fig. 2b and c. For this, the bathymetry was a transect taken from the near-field model and calculations were performed using a telescoped grid with horizontal and vertical resolutions of 7.8 m and 6.1 m, respectively. None of the models explicitly resolve the three-dimensional turbulence that is directly responsible for model energy dissipation.

The two Kuroshio models used are different implementations, but similar in their resolution, intent and skill. One (Fig. 4a, vectors) is an application of the NRL Ocean Nowcast/Forecast[37–39], an integration of the Navy Coastal Ocean Model (NCOM) and a statistical data-analysis model. In addition to the tidal forcing, the model's open boundary conditions are from a larger-scale model for the entire east Asian seas[40]. The second model, used to generate the ray paths (Fig. 4c, red/blue meshes), is a data-assimilating version of the Hybrid Coordinate Ocean Model (HYCOM)[41].

Shipboard measurements. The basic physical quantities required to characterize physical ocean flows are the potential density (density with the compression effects of hydrostatic pressure removed) and velocity. The former is measured with conductivity, temperature and depth instruments (CTDs) that are repeatedly lowered and raised from a shipboard winch. Salinity S is computed from temperature T, conductivity and pressure P measurements, and density is then a function of salinity, temperature and pressure. Velocity is measured with acoustic Doppler current profilers (ADCPs). These are affixed to the hull of the ship or lowered with the CTD instrument, and velocity is measured as a function of depth beneath the ship by the phase shift of 75-kHz, 150-kHz or 300-kHz acoustic pulses backscattered from the water column. The precision of CTD and ADCP measurements depends on set-up and several other factors. Typical uncertainties for density and velocity are 2×10^{-4} kg m^{-3} and 0.01 m s^{-1}, respectively, which are one to two orders of magnitude less than the signals described here. The energy flux measurements presented in Fig. 2a (flux calculation described next) are computed from 36-h time series stations wherein velocity and pressure are repeatedly measured by cycling the CTD up and down approximately once each hour. The measurements in Fig. 2e are from a specialized 'fast CTD' system[18] designed to sample much faster than a conventional CTD (a profile approximately every ten minutes as opposed to about every hour, depending on water depth).

Glider measurements. Measurements of energy flux were made from autonomous gliders[42] as part of IWISE (Fig. 1c). Gliders are autonomous underwater vehicles that move up and down through the water by adjusting their buoyancy, which is accomplished by filling and draining oil from a bladder. Wings allow the glider to 'fly' through the water at about 0.25 m s^{-1}. During IWISE, two gliders were deployed for about two months each, and sampled density and velocity in the upper 500 m every 3 h.

Moored measurements. Three types of moored measurements were made during IWISE: (1) Profiling moorings featuring a McLane Moored Profiler[43] crawling up and down a vertical moored wire approximately every 1.5 h between 300 m and 400 m below the surface and about 10 m above the bottom. Above, a series of approximately 30 densely spaced temperature loggers and an ADCP gave temperature (from which density was computed) and velocity in the upper ocean. The moored profilers carried current meters and CTDs, giving continuous, full-water-column measurements of density and velocity from a mooring, a challenging task.

(2) ADCP/T-chain moorings held ADCPs and made temperature and/or salinity measurements, giving faster sampling at the cost of vertically continuous data. Both of these types of moorings were prone to substantial knockdowns by the extreme currents in Luzon Strait. Knockdowns were minimized by highly taut designs and (for one mooring) a low-drag cylindrical float. When they occurred (up to 100 m in the worst case), they were corrected for by means of pressure measurements on the top subsurface floats.

(3) A final moored measurement used bottom-mounted pressure inverted echo sounders (PIES), which measure bottom pressure and the round-trip bottom–top–bottom travel time of an acoustic pulse transmitted upward every few seconds. Since sound speed depends on temperature, these signals are proportional to the mode-1 displacement of the thermocline[44]. True mode-1 displacements in Fig. 4a and b were computed from travel time using nearby moored *in situ* temperature measurements, and have an overall uncertainty of 4 m (ref. 44).

Turbulence measurements. The turbulence measurements described on the continental shelf were obtained directly using a Rockland Vertical Microstructure Profiler. The turbulent dissipation rate ε was estimated by fitting small-scale velocity shear observations to a theoretical spectrum and integrating by following the method of ref. 45. The turbulent dissipation results in Fig. 2d were obtained indirectly using the method of overturns or "Thorpe sorting"[46], which computes the outer scale of the turbulence via the vertical distance parcels of water have moved from a stably stratified profile. Numerous previous studies[46–48] have demonstrated good agreement with direct measurements; although recent modelling work[49] has given rise to the possibility that Thorpe-based estimates could be biased high by a factor as great as 2 to 6.

Synthetic aperture radar imagery. Although nonlinear internal waves propagate in the interior of the ocean, their currents produce convergent (rough) and divergent (smooth) zones on the ocean surface that move in phase with their subsurface crests and troughs. These variations in surface roughness create the distinctive light/dark pattern of the internal wave packets found in synthetic aperture radar images of the ocean (Fig. 1b), which have a typical horizontal resolution of tens of metres. The technique is sensitive to the background roughness of the sea surface, which depends on wind speed and other factors. Therefore, imagery is an excellent indicator of the location and morphology of the wave fronts, but generally cannot give wave amplitude.

Energy flux. The internal tide energy flux F (presented in Figs 2a and 3a, b) is computed from both model and observed data as the depth integral of $<\boldsymbol{u}'p'>$, where $\boldsymbol{u}'$ is the measured velocity fluctuation with the barotropic tide removed and p' is the baroclinic pressure, computed from the density assuming hydrostatic balance[50].

Energy flux is computed separately for the semidiurnal and diurnal motions by use of harmonic analysis. Shipboard time-series stations are always conducted for $\geq$36 h, allowing separation of these motions from each other and from the inertial frequency, which is 33.4 h at this latitude. For each 36-h station or 3-day time period in the case of moored and glider data, least-square fits are done at each depth to semidiurnal, diurnal and inertial motions. Much longer time series ($\sim$14 days) would be required to separate the different tidal constituents within each band (for example, M2/S2 and K1/O1), so the diurnal and semidiurnal motions are referred to as D1 and D2, respectively.

Nonlinear coupling between different frequencies would complicate our method of separation into bands. To ensure that nonlinear terms are not important in this context, the sum of the separated fluxes is compared to the total flux before separation. The two agree to within 10%[15,17,51].

Because it requires a vertical integral, the calculation of p' relies on full-water-column data. Therefore, gaps in the water column measurements give rise to errors, particularly when they are near the surface where the flux is the greatest. For the model data and CTD/ADCP station measurements (Fig. 2a) gaps and associated errors are negligible. For the moored measurements where gaps are only tens of metres out of thousands, the associated errors are about 20%[51,52], which are determined by sampling the full-water-column model output with the coverage of the moorings. For the glider measurements, which sample only the upper 500 m, calculation of energy flux relies on fitting the data to the first baroclinic mode. Although the moored data verify that the bulk of the energy is in this mode, glider uncertainty in total flux is about 30%[53].

To account for modulation by the spring/neap cycle, flux values from 36-h stations are converted to time-mean values by scaling them with the square of the barotropic velocity during the time of observations[15]. Values from moorings, which directly measure this modulation, are simply the time-mean for each constituent.

The energy flux of nonlinear waves (presented in Fig. 3c) has two extra terms in addition to the linear term computed above for the internal tides. An accurate expression for the energy flux of nonlinear waves is cE, where c is the wave speed and E is the sum of their kinetic and available potential energy[54]. The

nonlinear waves' short timescales (minutes as opposed to hours for the internal tides) enables them to be easily isolated from the internal tides by means of bandpass filtering.

Energy budget calculation. Although in general internal wave energy arises from a combination of wind and tidal forcing, in Luzon Strait the dominant energy source is the barotropic tide. Conversion from barotropic tidal motions to baroclinic energy can be quantified as $C = U_{BT} \nabla H p_{bot}$, where U_{BT} is the barotropic tidal velocity, H is the seafloor depth and p_{bot} is the pressure at the seafloor. Though observations can be used to compute conversion[55], they are far too sparse to estimate the integral over the near-field region, so we use the model (uncertainties presented below).

In steady state, an energy budget for the internal tides (which here we consider to be comprised of only the nearly sinusoidal waves) can be written as

$$C - \nabla F = D \quad (1)$$

where D represents all processes removing energy from the internal tide, including dissipation and transfer of energy to the sharp nonlinear waves seen to the west. In the near-field region where no nonlinear waves are yet present, D represents primarily turbulent processes. In the west, reductions in internal tide flux also arise as nonlinear wave fluxes increase (Fig. 3c).

None of the models resolve turbulence. However, the two- and three-dimensional near-field models resolve the processes that lead to it, primarily breaking internal waves, as shown in Fig. 2. Dissipation in these models is computed from a closure scheme[56] similar to the above Thorpe sorting algorithm used in the measurements. Observed and modelled dissipation have been demonstrated to be within a factor of two of one another in breaking lee waves observed at several sites in the Luzon Strait[17] and one at the Hawaiian Ridge[57], but a detailed comparison at Luzon Strait is not yet complete.

The integrated conversion and fluxes discussed in the main text are computed by integrating the far-field model (Fig. 3a, b) over the domain (19°–21.5° N, 120°–122.5° E). Flux and dissipation values plotted in Fig. 3c are all from measurements near 21° N[29,58,59]. Measurements along a line rather than integrated values are subject to reduction by cylindrical spreading. As is evident in Fig. 3a and b, the model shows a factor-of-two reduction in fluxes along 21° N for D1 and a <20% reduction for D2, owing to differences in their generation geometry.

Measurements at 120° E are from gliders, which agree well with the far-field model[53]. Internal tide and nonlinear internal wave flux estimates further to the west are from moorings. Turbulence estimates on the continental slope and upper shelf are from Thorpe scales, while those west of 117.25° E are directly measured with the Vertical Microstructure Profiler. The separate eastward and westward fluxes from the mooring at 117.895° E are estimated by assuming the continental slope is a vertical wall (a good assumption for the diurnal motions); the separate fluxes are then estimated from the ratio of the total energy to the flux with knowledge of the distance between the mooring and the wall.

Integrated dissipation on the slope and shelf is computed from the available observations by simply integrating with respect to depth and multiplying by the cross-slope distances indicated in Fig. 3c, which assumes that the observed locations are representative. Because the validity of this assumption is not known, the estimates are uncertain by at least a factor of two.

Model uncertainty. The skill of the models is evaluated by first comparing energy flux estimates point-by-point with observations, and then comparing integrated conversion and energy flux between the different models. Far-field model and observed flux magnitude are generally within a factor of two of each other, with flux direction agreeing to about 30° (Extended Data Fig. 1). Modelled D2 fluxes are about twice the observed values at the northern stations (N1, N2, LS02; see ref. 15 for station locations), suggesting the possibility of a high bias in the model in that region. However, glider and far-field model values just west of these stations are in agreement[53], suggesting instead that the poorer agreement at these stations may be due to the extremely steep slopes at those locations.

Additional uncertainty arises from the energy difference between the models, which is also approximately a factor of two (Extended Data Table 1). Specifically, near-field conversion and radiated flux in the near-field model exceed those in the far field and Kuroshio models by nearly a factor of two, probably because of the near-field model's higher resolution. All three models have very similar spatial patterns, consistent with those inferred from observations (Fig. 2a; refs 15, 17). Taking into account the factor-of-two scatter between the observations and the far-field model, and this factor-of-two energy difference between the different models, we choose to use the far-field model in the energy budget calculation, and estimate an overall factor-of-two uncertainty in all model flux and conversion estimates.

Data. Source data for each figure are provided as spreadsheets online.

31. Egbert, G. & Erofeeva, S. Efficient inverse modeling of barotropic ocean tides. *J. Atmos. Ocean. Technol.* **19,** 183–204 (2002).
32. Smith, W. H. F. & Sandwell, D. T. Global sea floor topography from satellite altimetry and ship depth soundings. *Science* **277,** 1956–1962 (1997).
33. Teague, W. J., Carron, M. J. & Hogan, P. J. A comparison between the generalized Digital Environmental Model and Levitus climatologies. *J. Geophys. Res.* **95,** 7167–7183 (1990).
34. Hallberg, R. & Rhines, P. Buoyancy-driven circulation in an ocean basin with isopycnals intersecting the sloping boundary. *J. Phys. Oceanogr.* **26,** 913–940 (1996).
35. Simmons, H. L. *et al.* Modeling and prediction of internal waves in the South China Sea. *Oceanography* **24,** 88–99 (2011).
36. Marshall, J., Adcroft, A., Hill, C., Perelman, L. & Heisey, C. A finite-volume, incompressible Navier Stokes model for studies of the ocean on parallel computers. *J. Geophys. Res.* **102** (C3), 5753–5766 (1997).
37. Ko, D. S., Martin, P. J., Rowley, C. D. & Preller, R. H. A real-time coastal ocean prediction experiment for MREA04. *J. Mar. Syst.* **69,** 17–28 (2008).
38. Chen, Y.-J., Shan Ko, D. & Shaw, P.-T. The generation and propagation of internal solitary waves in the South China Sea. *J. Geophys. Res. Oceans* **118,** 6578–6589 (2013).
39. Ma, B. B., Lien, R.-C. & Ko, D. S. The variability of internal tides in the Northern South China Sea. *J. Oceanogr.* **69,** 619–630 (2013).
40. Ko, D. S., Martin, P. J., Rowley, C. D. & Preller, R. H. A real-time coastal ocean prediction experiment for MREA04. *J. Mar. Syst.* **69,** 17–28 (2008).
41. Chassignet, E. P. *et al.* The HYCOM (HYbrid Coordinate Ocean Model) data assimilative system. *J. Mar. Syst.* **65,** 60–83 (2007).
42. Sherman, J., Davis, R., Owens, W. & Valdes, J. The autonomous underwater glider "Spray". *IEEE J. Oceanic Eng.* **26,** 437–446 (2001).
43. Doherty, K., Frye, D., Liberatore, S. & Toole, J. A moored profiling instrument. *J. Atmos. Ocean. Technol.* **16,** 1816–1829 (1999).
44. Li, Q., Farmer, D. M., Duda, T. F. & Ramp, S. Acoustical measurement of nonlinear internal waves using the inverted echo sounder. *J. Atmos. Ocean. Technol.* **26,** 2228–2242 (2009).
45. Gregg, M. C. in *Physical Processes in Lakes and Oceans* (ed. Imberger, J.) Vol. 54 305–338 (American Geophysical Union, 1998).
46. Dillon, T. M. Vertical overturns: a comparison of Thorpe and Ozmidov length scales. *J. Geophys. Res.* **87,** 9601–9613 (1982).
47. Ferron, B. H., Mercier, H., Speer, K., Gargett, A. & Polzin, K. Mixing in the Romanche fracture zone. *J. Phys. Oceanogr.* **28,** 1929–1945 (1998).
48. Alford, M. H., Gregg, M. C. & Merrifield, M. A. Structure, propagation and mixing of energetic baroclinic tides in Mamala Bay, Oahu, Hawaii. *J. Phys. Oceanogr.* **36,** 997–1018 (2006).
49. Mater, B. D., Schaad, S. M. & Venayagamoorthy, S. K. Relevance of the Thorpe length scale in stably stratified turbulence. *Phys. Fluids* **25,** 076604 (2013).
50. Althaus, A., Kunze, E. & Sanford, T. Internal tide radiation from Mendocino Escarpment. *J. Phys. Oceanogr.* **33,** 1510–1527 (2003).
51. Pickering, A. I., Alford, M. H., Rainville, L., Nash, J. D. & Lim, B. Spatial and temporal variability of internal tides in Luzon Strait. *J. Phys. Oceanogr.* (in the press).
52. Nash, J. D., Alford, M. H. & Kunze, E. Estimating internal-wave energy fluxes in the ocean. *J. Atmos. Ocean. Technol.* **22,** 1551–1570 (2005).
53. Johnston, T. M. S., Rudnick, D. L., Alford, M. H., Pickering, A. I. & Simmons, H. L. Internal tidal energy fluxes in the South China Sea from density and velocity measurements by gliders. *J. Geophys. Res.* **118,** 1–11 (2013).
54. Moum, J. N., Klymak, J. M., Nash, J. D., Perlin, A. & Smyth, W. D. Energy transport by nonlinear internal waves. *J. Phys. Oceanogr.* **37,** 1968–1988 (2007).
55. Kelly, S. & Nash, J. D. Internal-tide generation and destruction by shoaling internal tides. *Geophys. Res. Lett.* **37,** L23611 (2010).
56. Klymak, J. M. & Legg, S. M. A simple mixing scheme for models that resolve breaking internal waves. *Ocean Model.* **33,** 224–234 (2010).
57. Alford, M. H., Klymak, J. M. & Carter, G. S. Breaking internal lee waves at Kaena Ridge, Hawaii. *Geophys. Res. Lett.* **41,** 906–912 (2014).
58. Chang, M.-H., Lien, R.-C., Tang, T.-Y., D'Asaro, E. & Yang, Y.-J. Energy flux of nonlinear internal waves in northern South China Sea. *Geophys. Res. Lett.* **33,** 1–5 (2006).
59. St Laurent, L. C., Simmons, H. L., Tang, T. Y. & Wang, Y. H. Turbulent properties of internal waves in the South China Sea. *Oceanography* **24,** 78–87 (2011).

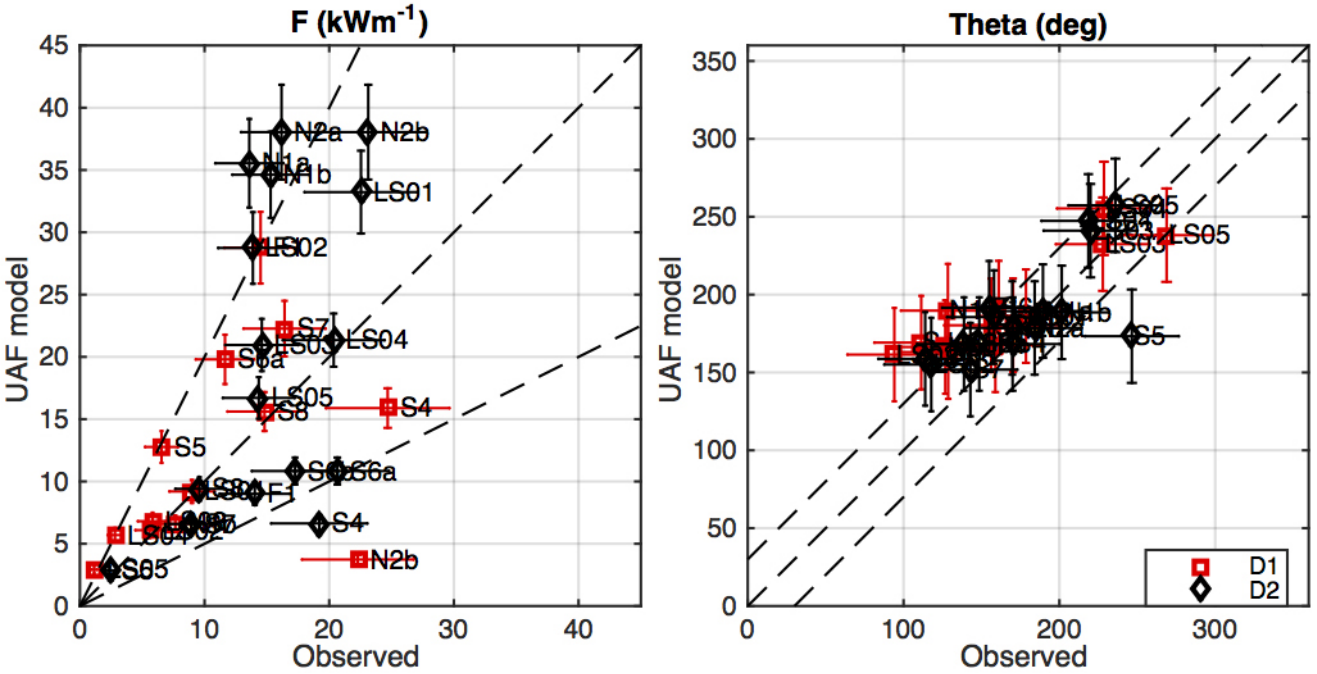

Extended Data Figure 1 | Comparison of observed and model energy flux. Left, Scatter plot of flux magnitude F from observations (x axis) and far-field (UAF; University of Alaska Fairbanks) model (y axis). Error bars are ±20% for observed values and ±10% for model values (see Methods). Right, As for the left panel, but for direction θ; error bars are ±30°. See source data and ref. 15 for station locations. Black, semi-diurnal; red, diurnal.

Extended Data Table 1 | Conversion and radiated flux integrated over the region 19° to 21.5° N, 120° to 122.5° E.

	Conversion / GW	Radiated Flux / GW
Near-field	43	23
Far-field	24	15
Kuroshio	-	14

-, Not resolved.